On the Impact of Operating Conditions and Testing Environment on the Noise Sources in an Industrial Engine Cooling Fan

On the impact of operating conditions and testing environment on the noise sources in an industrial engine cooling fan

Francesco Bellelli*, Renzo Arina† and Francesco Avallone‡
Politecnico di Torino, Torino, 10129, Italy

In the evolving automotive landscape, the shift from conventional thermal engines to electric ones has made unconventional noise sources more relevant, such as the engine cooling fan, especially from the human listener's point of view. The engine cooling module has therefore become of primary concern, leading to design studies for quieter and efficient fans. However, it has been shown that different testing conditions can widely alter the noise footprint of these fans; thus, the assessment of the installation's effect on different testing cases rapidly gained importance. This paper, therefore, investigates an industrial engine cooling fan's main noise sources and generation mechanisms. Installation effects in the semi-anechoic room and at two different operating points (free blowing and maximum efficiency) are numerically assessed. First, the fan is tested at free blowing conditions in a testing environment that resembles a semi-anechoic room. At free blowing conditions there's no pressure difference across the fan, with a high mass flow rate through it. As a consequence, being off-design condition, the flow over the blades is largely separated, locally recovering when the blade passes through a blockage region given by the motor cable strut. The noise footprint is therefore highly tonal, with a clear peak on the blade passing frequency tone. If the same fan is tested in a free field environment, it is found that there is a difference on the acoustic pressure at higher harmonics of the blade passing frequency. Then, the fan is tested at maximum efficiency. In this condition is found that the blockage mentioned above is no longer present, since a pressure difference is set, yielding a lower mass flow rate through the fan. The main noise generation mechanism can be instead found in the tip leakage vortex which arises because of the pressure difference across the fan and interacts with the blade tip leading edge, also resulting in a more broadband noise footprint. This highlights the importance of assessing the effect of the testing point on the fan's acoustics, since in the industry is a standard practice to test with zero pressure difference.

I. Nomenclature

BPF	=	Blade passing frequency
SPL	=	Sound pressure level
LBM	=	Lattice-Boltzmann method
VR	=	Variable Resolution
PSD	=	Power Spectral Density
FWH	=	Ffwocs-Williams and Hakwings
vox	=	Number of voxels in the finest VR region
D	=	Fan diameter
Ω	=	Fan angular velocity in RPM
N_b	=	Number of rotor blades
N_v	=	Number of stator vanes
Δp	=	Pressure difference across the fan
$\dot{m}$	=	Mass flow across the fan
$v_{tip} = \Omega D/2$	=	Tip velocity
ω	=	Vorticity

*Ph.D. student, Department of Mechanical and Aerospace Engineering, francesco.bellelli@polito.it
†Associate Professor, Department of Mechanical and Aerospace Engineering, renzo.arina@polito.it
‡Full professor, Department of Mechanical and Aerospace Engineering, francesco.avallone@polito.it

$p^{\circ}_{tip} = 1/2\rho v^2_{tip}$ = Tip dynamic pressure
$\psi = \frac{2\Delta p}{\rho v^2_{tip}}$ = Load coefficient
$\varphi = \frac{4\dot{V}}{\pi(D^2 - D^2_{hub})v_{tip}}$ = Flow coefficient
$c_p = \frac{p - p_{amb}}{0.5\rho_{amb} v^2_{tip}}$ = Pressure coefficient

II. Introduction

Given the need to be cooled, automotive thermal engines and electric motors need a cooling fan package. Its first design purpose has always been aerodynamic efficiency, but since quieter electric motors are replacing thermal engines in the consumer automotive industry, they also need to lower noise emissions. As expected, research on noise generation mechanisms and reduction techniques rapidly gained importance in industry and academia [1, 2]. Also, the increasingly severe regulations on noise emissions that arose in the past years reinforced this trend. Researchers have therefore put their effort into delineating the most concerning noise generation mechanisms and, on the other hand, which noise reduction solutions can be both affordable and efficient.

These rotating machines have a wide variety of possible noise sources, starting with the more conventional, until ones that are intrinsically related to complex physical mechanisms.

The first noise generation mechanism is the so-called thickness noise, due to the air displacement induced by blade passage. Although the pressure fluctuations caused by this mechanism are often negligible for low Mach numbers, it has been shown that for high-solidity fans this contribution can be relevant [3]. Under the hypothesis of a steady and uniform inflow, a fixed observer also sees a pulsating force (blade loading) with a frequency $f = N_b\omega$, where $\omega = \Omega/60$ is the fan rotational frequency, called blade passing frequency (BPF). These two mechanisms result in a sharp peak in the acoustic pressure spectrum at the BPF. A commonly adopted solution to distribute this peak on a broader frequency range is unevenly spacing fan blades [4].

If, on the other hand, the inflow is unsteady or not uniform [5], its interaction with the blade leading edge causes an unsteady blade loading fluctuation that results in peaks at the BPF and its harmonics, as well as a broadband footprint on the acoustics. To reduce this contribution, several solutions have been studied. Firstly, the blade leading edge can be redesigned with a wavy [6] or slitted [7] profile (sometimes bionic-inspired [8]) to decorrelate the incoming turbulent structures. However, this might enhance pressure fluctuations at higher frequencies. Secondly, a fine-tuned short inlet duct [9] has been used to homogenize the incoming turbulent structures in the azimuthal direction. Porous materials [10] can also be used to weaken the inflow turbulence noise, but they might clash with the industrial feasibility.

Since the vast majority of these cooling fans is equipped with several stator vanes, tonal noise from the interaction between rotor blades and stator vanes occurs. The noise can be due to the potential effect of the stator vanes on the blades, or it can arise from the impingement of the blades' wake on the stator vanes. By unevenly spacing both rotor blades and stator vanes it has been seen [11] that tones at BPF and harmonics can be lowered; this, however, is not always verified if the operating conditions are different from the design ones. It has been also seen that an azimuthal heterogeneity on the stator vanes [12, 13] can result in a higher tonal contribution, with the rise of additional azimuthal modes beyond the ones predicted with the Tyler and Sofrin rule [14]. However, in industry, such a design, in which possible heterogeneities are present, is often unavoidable.

Finally, a relevant noise generation mechanism is the so-called tip clearance noise, which is addressed to the interaction between the blades and the coherent vortex structures [15] that are generated in the gap between blades and shroud. Its contribution to the far-field acoustics can be found in the sub-harmonic humps which can be seen on the spectrum [16] because of the backflow due to the pressure difference across the fan [17]. These vortex structures can be weakened by the forward sweeping of the blades [18] and by introducing a rotating [19], and even a stationary [20], ring on the rotor.

Other studies pointed out the noise reduction properties of a bell-mouth inlet [21, 22] that, however, might not be industrially suitable due to higher encumbrance, and of adopting casing treatments [23]. The latter aims to locally reduce tip clearance (i.e. weaken the coherent vortex structures generation) but its effect isn't clear and it can suffer industrial feasibility too.

It is clear that "academic" and industrial low-speed axial fans show substantial differences in their design and in the noise reduction solutions that they adopt. From an industrial perspective, what is seen to be effective may not be efficient, considering that a cooling module might perform in a different environment and a different working condition. Furthermore, the integration of the various components of a cooling module might generate additional interactions

which contribute to the far-field noise [24]. Another noteworthy point is that industrial products must be certified in specific conditions. It has been shown in literature [25, 26] how the flow recirculation in the testing chamber (related to the moderate extension of the experimental facilities with respect to the actual working environment of the fan) has a noticeable impact on the sound emission, despite the flow field and the loading history might show negligible discrepancies. Moreover, Longhouse [27] showed how the noise sources can exhibit significant differences when the operating point is changed. Indeed, standard industry practice is testing with zero pressure difference across the fan (often referred to as the free blowing condition), mainly due to the economical and complex aspects of building an anechoic wind tunnel. Hence, the fan is often tested in a non-representative working condition, thus showing different noise generation mechanisms with respect to the real working case.

This paper, therefore, aims to characterize the noise sources of an industrial engine cooling fan by assessing the installation effects on the sound generation mechanisms, focusing on the sensitivity of the noise generation mechanisms under different conditions, including variations in the testing environment from a semi-anechoic chamber to a free field ambient, and changes in the fan's operating point from free blowing to maximum efficiency conditions. The former means that there isn't any pressure difference across the fan, thus yielding a high mass flow rate through it, while the latter means that a pressure difference is instead established, subsequently resulting in a lower mass flow rate.

The present paper is structured as follows: Section III presents the used methodology to calculate hydrodynamic and acoustic fields numerically. Section IV summarizes briefly the experimental setup used to validate the numerical calculations, which are presented in detail through section V. The grid convergence study on the numerical counterpart of the experimental setup is discussed in Section VI. Section VII discusses the obtained results, while the main conclusions and future works are highlighted in section VIII.

III. Methodology

The flow field is numerically simulated with PowerFLOW version 6 by 3DS, based on the Lattice-Boltzmann method [28]. As a commercial CFD code, it has been widely used to study the aerodynamics and aeroacoustics of low-speed fans for automotive applications such as in References [18, 29–31].

The continuous Boltzmann equation is:

$$\frac{\partial f}{\partial t} + c\frac{\partial f}{\partial t} + \frac{F}{m}\frac{\partial f}{\partial c} = \Omega \tag{1}$$

Here $f(\vec{x}, \vec{c}, t)$ is the particle distribution function, which represents the probability that at time t there is a particle at position $\vec{x}$ with microscopic velocity $\vec{c}$. F is the external force, m is the molecular weight of the fluid, and Ω is the so-called collision operator, which accounts for the distribution function variation due to elastic collisions between two particles. Since the collisions are elastic, then mass, momentum, and kinetic energy must be conserved. By further modeling the collision operator with the one called BGK (Bhatnagar, Gross, Krook) [32] and performing a Chapman-Enskog expansion [33], it is possible to recover the Navier-Stokes equations from Eq. 1 for low Mach numbers.

The Boltzmann equation is numerically discretized, recalling that the BGK collision operator is

$$\Omega = -\frac{1}{\tau}(f - f^{eq}), \tag{2}$$

where τ is the relaxation time and f^{eq} is the equilibrium distribution function, to which f tends. The equilibrium distribution function is modeled with the Maxwell-Boltzmann one. First, discretization in space and time is done by dividing the computational domain into cubic lattices, called voxels. In every voxel, particles are set to move only in a fixed number of directions (in its low Mach number solver, PowerFLOW implements a model with 19 discrete velocities [34]). The discretized Boltzmann equation is then written for every voxel and further solved through two subsequent steps: collision and streaming on the near neighbors. To consider the possibility of simulating rotating parts, a sliding mesh approach is used [35].

To directly resolve only the turbulence scales beyond a certain threshold, a Very Large Eddy Simulation (VLES) formulation is used. This can be done by adjusting the relaxation time further including a contribution arising from the spatial filtering; furthermore, the effective relaxation time can be written as

$$\tau_{eff} = \tau + \tau_{turb} \tag{3}$$

The implemented subgrid model is derived from the renormalization group $k - \epsilon$ transport equations (RNG $k - \epsilon$) [36]. To further reduce the computational cost, the flow field in the vicinity of solid walls is approximated through the

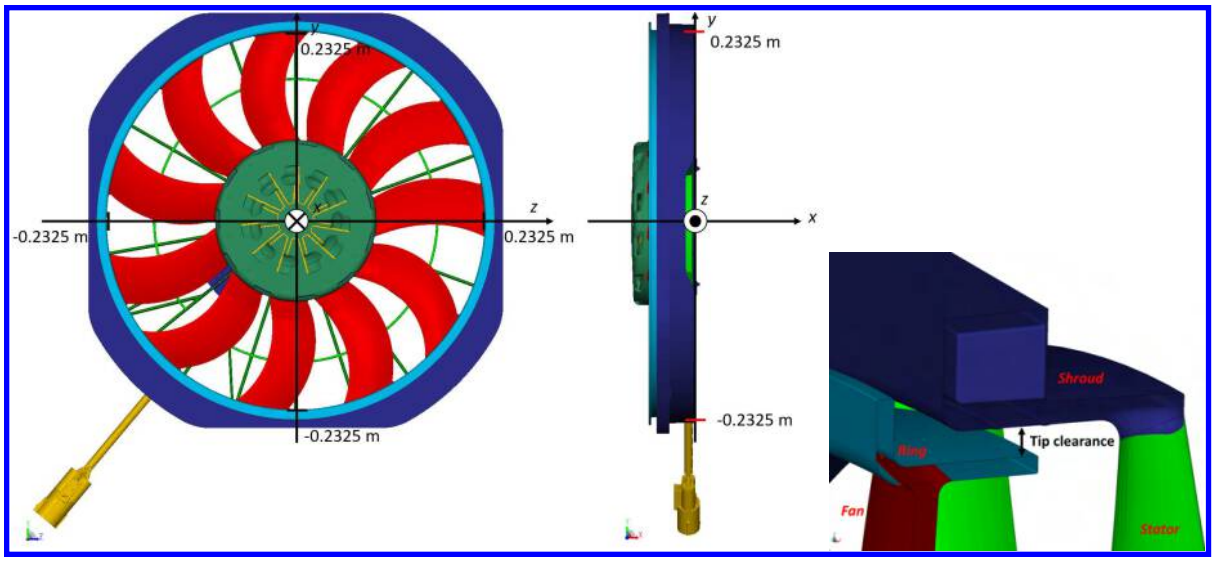

(a) **(b)**

Fig. 1 Tested automotive engine cooling module. The main parts in which the fan consists are shown with different colors. (a): Cooling module. (b): Tip clearance detail.

Fan diameter	Tip clearance	N_b	N_v	RPM	ψ
465 mm	6.46% blade tip chord	11	20	3048	0

Table 1 Experimental parameters.

pressure-gradient extended wall model (PGE-WM) [37], an extension of the generalized wall model by Launder and Spalding [38].

The advantages of LBM rely upon the fact that is not necessary to generate complex and unstructured grids since the computational domain is simply divided cubic lattices, and that is a highly parallelizable method, due to the explicit time-marching method that is used to solve numerically Eq. 1. LBM is particularly suited for aeroacoustic applications since it allows for direct aeroacoustic computation in the flow field. This is possible thanks to the lower numerical diffusion and dispersion against the most common CFD schemes based on the Navier-Stokes equations. Indeed, 15 vox per wavelength are sufficient to directly compute the acoustic signature from the unsteady flow field.

The far-field acoustics is therefore directly computed from the pressure fluctuations recorded at specific locations as will be further discussed in Sec. V. To further discriminate the contribution of each solid surface on the far-field noise, FWH acoustic analogy [39] is applied with a forward-time solution [40] based on formulation 1A by Farassat [41].

IV. Experimental setup

The automotive engine cooling module consists of a fan, a rotating ring, a hub, a driving electrical motor, the stator vanes, and a shroud, as shown in Fig. 1a with different colors. The main geometrical and physical parameters are summarized in Tab. 1; since the fan is an industrial product, the performances are reported using non-dimensional parameters. The fan blows inside an anechoic room, therefore the free-blowing conditions apply. Experiments have been performed in a semi-anechoic chamber, which is a $5 \times 5 \times 3\,m$ semi-anechoic room equipped with an array of 7 equally spaced far-field microphones placed in an arc of $2.15D$ radius upstream of the fan, which is situated in the middle of the chamber.

V. Numerical setup

The computational setup is composed of a cubic simulation volume with solid walls as boundaries. The length of the domain boundaries is determined according to the resolution (in vox/D). The floor is at a distance of $3.22D$ from

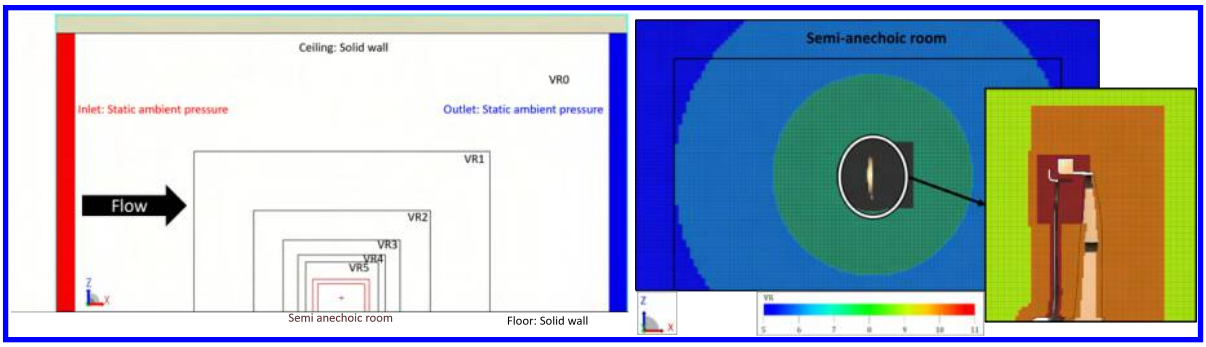

(a) **(b)**

Fig. 2 Numerical setup implemented in PowerFLOW. (a): Computational domain (free blowing conditions in the semi-anechoic room). The floor has been omitted from the picture. (b): Detail of the 11 VR regions. They are the same in all the simulated cases.

the fan center. Inlet and outlet walls are set to have ambient pressure and free field direction. Other walls are modeled as standard walls.

The semi-anechoic chamber walls are modeled as an equivalent porous medium (viscous resistance of 50000 $1/s$ in the three cartesian directions). The entire fan system CAD geometry has been imported; it, however, does not take into account the heat exchanger. The simulated cooling module is composed of 11 fan blades, 20 stator vanes, a motor, and a shroud, as in the experiments (Fig. 1a, Tab. 1).

To achieve accurate flow detail in the near field, while maintaining an affordable computational cost, 11 variable resolution (VR) regions are used. The voxel size of a specific VR region is twice the voxel size of the previous one. The resolution is set as the number of voxels per characteristic length so that the voxel size in the finer VR region is uniquely defined. Three simulations have been performed at three different resolutions of 600 vox/D, 1000 vox/D, and 1200 vox/D, to investigate grid convergence. The rotating motion of the blades is taken into account using a local reference frame in a sliding mesh approach, while the shroud and motor are modeled as solid stationary parts.

Pressure and velocity are sampled in two perpendicular planes located respectively at $y/D = 0$ and $z/D = 0$ at 48 kHz in order to obtain significant information both on the aerodynamics and aeroacoustic fields. Three planes parallel to the fan disk and located at $x/D = -0.1183$, $x/D = -0.0645$, and $x/D = 0$ are then sampled at 3 kHz to compute phase lock quantities, while a small volume around the cooling module is sampled at 755 Hz. The entire cooling module surface is sampled at 48 kHz and is used as an integration domain for the surface integral in the FWH acoustic analogy, with a solid formulation.

Furthermore, integral quantities such as blade loading, torque, and mass flow rate are sampled. Loading and torque are recorded every 4 timesteps, while the mass flow is sampled with a frequency of 48 kHz in the three planes located at $x/D = -0.1677$, $x/D = -0.0744$, and $x/D = 0$.

Finally, an array of 12 far field probes $2.15D$ far from the fan center is present, aiming to reproduce the experimental measuring points and provide further insights during the simulation process. A physical time of 20 revolutions is simulated for every condition.

The effect of a free field domain (i.e. not considering the actual semi-anechoic room testing facility anymore) is assessed by removing the aforementioned porous medium and setting the floor height equal to the ceiling one, as shown in Fig. 3a. Furthermore, the effect of a different operating point of the fan is accounted for by placing a solid thin wall across the fan, as shown in Fig. 3b, and by changing the initial pressure upstream of the fan from ambient pressure p_{amb} to $p_{amb} - \Delta p$; in addition, the inlet boundary condition is changed into a constant mass flow value. This last testing condition can be considered representative of a large anechoic wind tunnel where, however, the investigated cooling module has not been tested yet. Tab. 2 summarizes all the different numerical conditions that have been simulated (green cells indicate simulated conditions and red cells indicate combinations that haven't been calculated).

VI. Grid convergence and numerical setup validation

As a first step, it has been established the resolution for which grid independence is achieved; this is done for the semi-anechoic domain at free blowing conditions. The integral quantities (mass flow rate through the fan section, torque

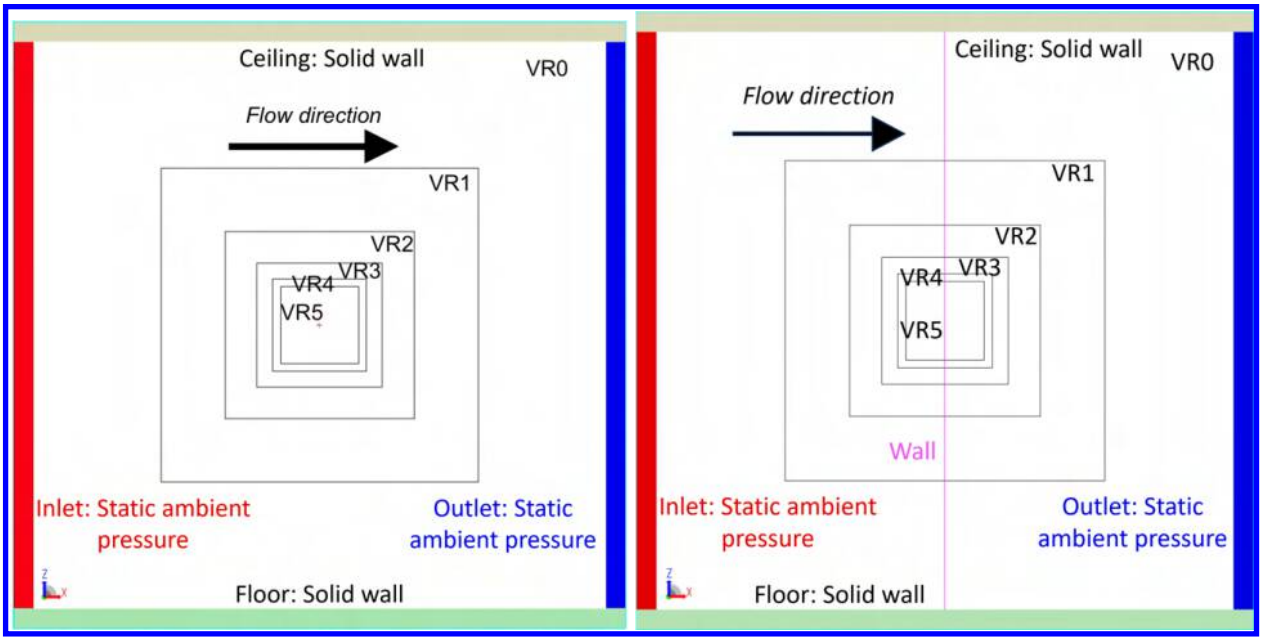

(a) **(b)**

Fig. 3 Description of the free field domains. (a): Sketch of the free field domain used for the free blowing case to compare against the semi-anechoic environment. (b): Sketch of the thin wall across the fan used in the free field domain to compare the free blowing case against the maximum efficiency operating point.

		Operating parameters			Numerical domain	
		ψ	φ	Ω	*Semi-anechoic*	*Free field*
Operating conditions	*Free blowing*	0	0.19	3048 *RPM*		
	Max efficiency	0.14	0.10	2868 *RPM*		

Table 2 Simulated conditions.

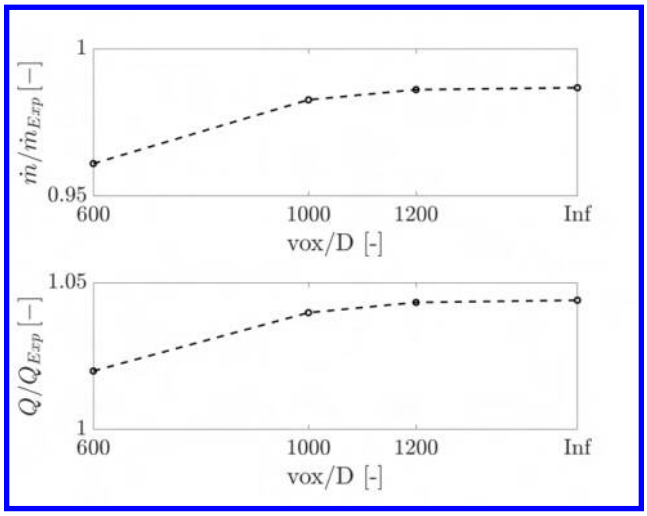

Fig. 4 Integral quantities along the three simulated resolutions, with respect to the experimental values.

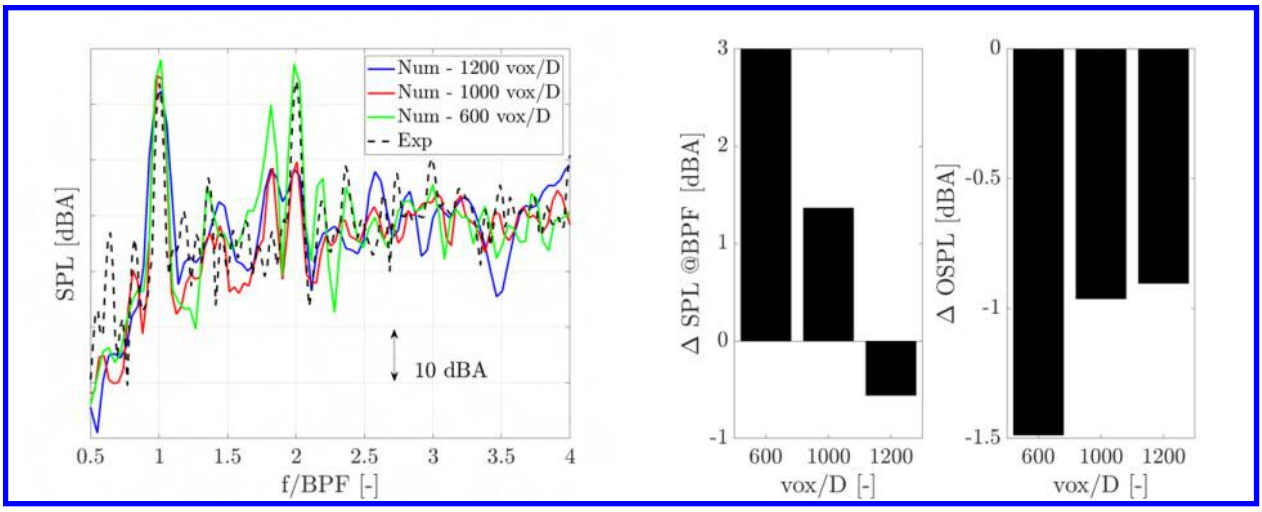

(a) **(b)**

Fig. 5 Grid independence study (semi-anechoic chamber, free blowing conditions). (a): Pressure fluctuations $2.15D$ upstream along the fan axis for both experiments and the three numerically simulated resolutions in vox/D. (b): SPL values at $f/BPF = 1$ and overall in the frequency range $0 \leq f/BPF \leq 4.5$.

on the impeller) referred to the experimental values for the three studied resolutions are shown in Fig. 4, in which "Inf" values are obtained through a Richardson extrapolation [42]. The finest resolution is sufficiently close to the asymptotic prediction, thus it can be stated that convergence is reached for $1200\,vox/D$. Indeed, it can be seen how the finest resolution can predict the mass flow within an error of 1 %; the torque, however, overestimated within 5%. Although this discrepancy, its value can be considered sufficiently accurate, as suggested by similar works in the literature [43].

The far-field noise spectrum measured $2.15D$ upstream on the fan axis is shown in Fig. 5a, while SPL at $f/BPF = 1$ and OSPL differences with respect to the experimental values are shown in Fig. 5b. A good agreement between experiments and numerical calculations is evident in Fig. 5a; the BPF tone can be correctly predicted within $3\,dBA$ (as reported in Fig. 5b), while the tone at $f/BPF = 2$ is overestimated with $600\,vox/D$ and, then, underestimated with resolutions of $1000\,vox/D$ and $1200\,vox/D$. The broadband content is correctly predicted with the two finest resolutions, starting from a frequency of about $f/BPF = 0.75$. It can be recognized in Fig. 5b that the resolution of $1200\,vox/D$ slightly improves the OSPL value with respect to the experiments, so it can be concluded that the numerical setup with $1200\,vox/D$ can correctly predict the experimental results. The following numerical calculations will be therefore presented only for the latter resolution.

VII. Results and discussion

A. Noise sources identification and free field effect at free blowing conditions

The first step of the present work has been the identification of the dominant noise generation sources in the numerical setup that emulate the experimental conditions (semi-anechoic chamber, free blowing conditions); in the second step, numerical data from the semi-anechoic and free field domains are compared at free blowing conditions, to assess the effect of the free field environment on the noise sources and, therefore, on the far-field acoustics. The porous medium in the simulation setup has consequently been removed and the floor height set equal to the ceiling height, as discussed before.

1. Aerodynamic results

Fig. 6a shows the mean flow topology in the semi-anechoic chamber settings at free blowing conditions. It can be seen that flow recirculation is present and that the wake is convected downstream with high velocity. Fig. 6b shows that a substantial flow blockage occurs downstream of the fan, in the azimuthal region where the motor cable strut is located.

This locally alters the incidence that every blade sees when passing through there, as shown in Fig. 7a, where the

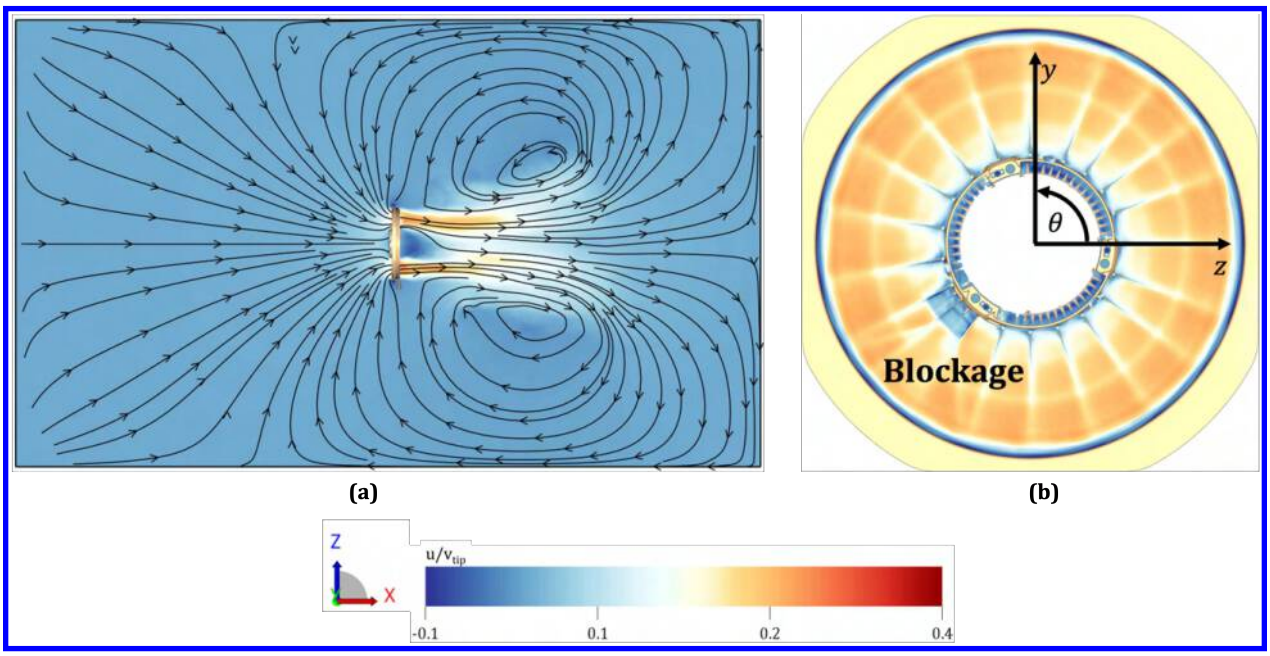

Fig. 6 Mean axial velocity (semi-anechoic chamber, free blowing conditions). (a): Mean flow topology in the semi-anechoic chamber in a plane located at $y/D = 0$. (b): Mean axial velocity in a plane located at $x/D = -0.06$.

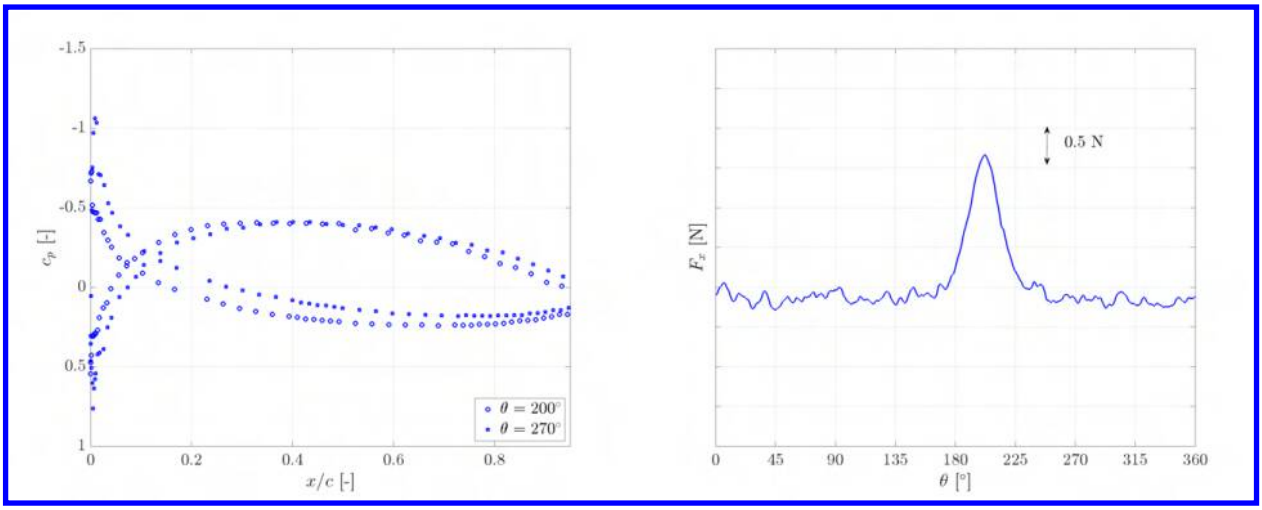

Fig. 7 Pressure coefficient and loading history of one blade (semi-anechoic chamber, free blowing conditions). (a): Pressure coefficient of one blade at two different θ locations. $\theta = 200°$ corresponds to the blockage region. (b): Loading history of one blade over a rotation cycle.

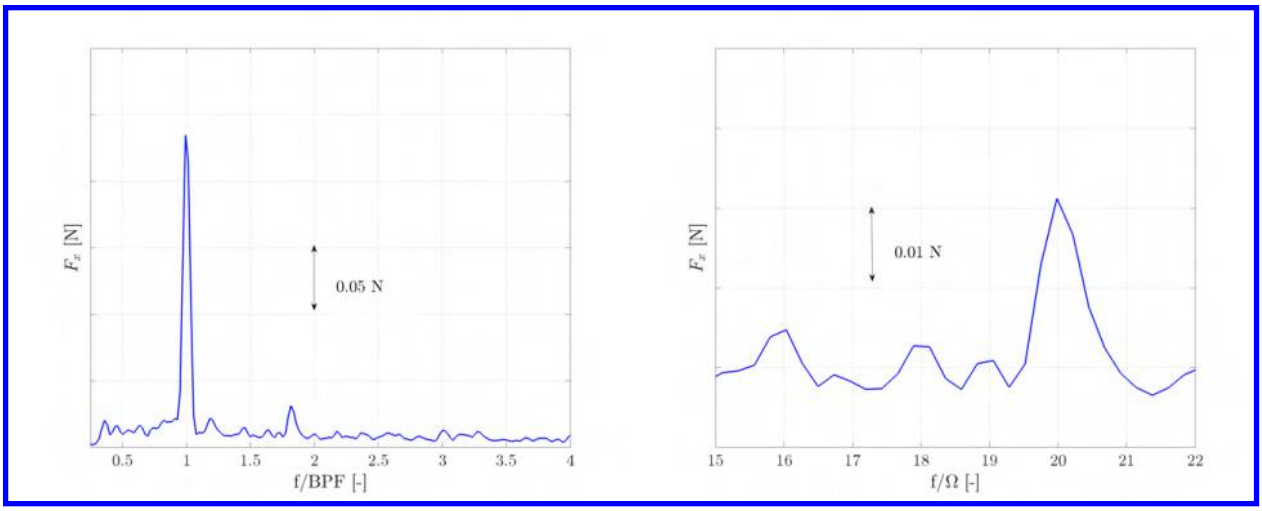

(a) **(b)**

Fig. 8 Blade loading spectra (semi-anechoic chamber, free blowing conditions). (a): Spectrum of the loading given by all the 11 blades. (b): Loading spectrum of one blade, the reference frequency here is the fan rotation frequency Ω.

pressure coefficient distribution exhibits an evident deviation compared to another θ location. The local incidence decrease is associated with a strong loading peak for each blade, as confirmed by the loading history in Fig. 7b.

Therefore, it will be generated a peak at the BPF for the entire blade ensemble, as visible in the blades' loading spectrum in Fig. 8a. The tone prominence is aggravated by the fact that the loading oscillation is severe since there is an azimuthally periodic transition between a nearly zero loading condition (separated flow over the blades) and a higher loading condition, corresponding to the moment when the blade overlaps the cable region, therefore the flow has a lower axial velocity and, finally, the incidence is reduced such that the flow over the blades is much less separated. Indeed, it can be seen in Fig. 7a that the flow over the blades is mostly separated. This occurs because the mass flow rate is higher with respect to the maximum efficiency case, and so is the axial velocity. Since the incidence for a rotating blade is roughly proportional to the ratio between axial and tangential velocity, the incidence seen by the blades in this off-design condition is higher than at maximum efficiency, yielding to a flow separation. In addition, a prominent sub-harmonic hump is visible at $f/BPF = 1.81$ in Fig. 8a and might be related to the presence of the 20 stator vanes that influence blade loading through the potential interaction between rotor and stator. As shown in Fig. 8b, every blade has a slight loading peak at a frequency $f/\Omega = 20$, resulting in a peak at a frequency of $f = 20\Omega/11 = 1.81BPF$.

The standard deviation of wall pressure on the fan in Fig. 9 points out the main fluctuations to be located on the blades' pressure side, on the stator vanes' leading edge, and the motor's cable strut on the shroud.

The switch from semi-anechoic to free field domain has the main consequence of removing all the flow recirculation that could be seen otherwise, as highlighted in Fig. 10, where the instantaneous vorticity field is shown. Indeed, the flow can now move in a much larger space (not entirely visible in the figure) and, therefore, the recirculation is severely reduced. Pressure fluctuations over the cooling module surface do not show any difference, yielding the same standard deviation and loading spectrum of the semi-anechoic chamber case. Therefore, there will not be shown the same results for the free field domain under free blowing conditions.

2. Acoustic results

An FWH analysis, using the solid formulation, has been performed on the cooling module at the frontal probe $2.15D$ upstream aligned with the fan axis. This makes, in addition, possible to discriminate the contribution of every solid part, at a specific microphone location; the geometry has been therefore divided into several parts, which are highlighted with different colors and summarized in Fig. 1a. Far-field acoustic spectra of each surface contribution and of the total contribution at the probe aligned with the fan axis $2.15D$ upstream are shown in Fig. 11. It can be observed a prominent tone at the BPF and a sub-harmonic hump at $f/BPF = 1.81$, as in the loading spectrum discussed before; it can also be seen that the contribution of the blades is highly dominant over the entire analyzed frequency range. Therefore, it can be

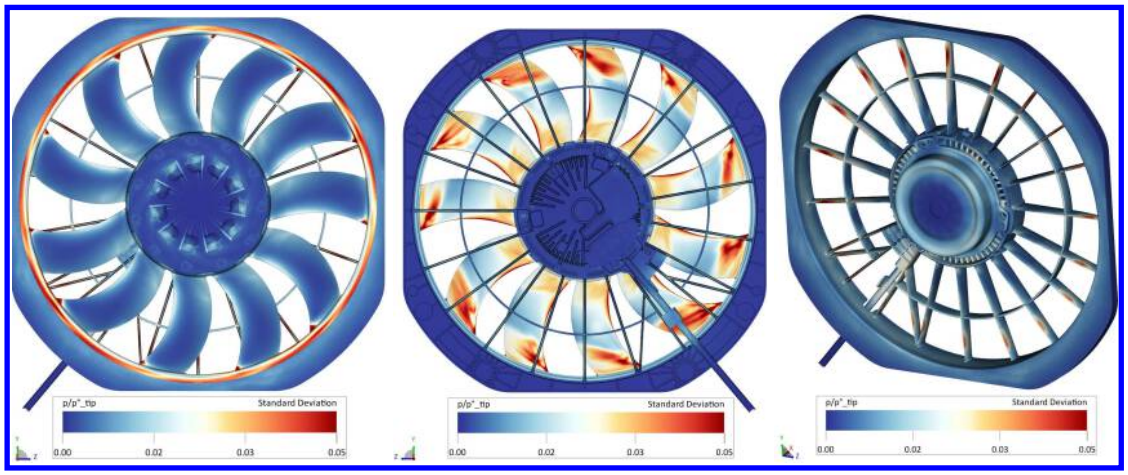

(a) (b) (c)

Fig. 9 Surface pressure standard deviation (semi-anechoic chamber, free blowing conditions). (a): Front plane. (b): Rear plane. (c): Isometry of the shroud.

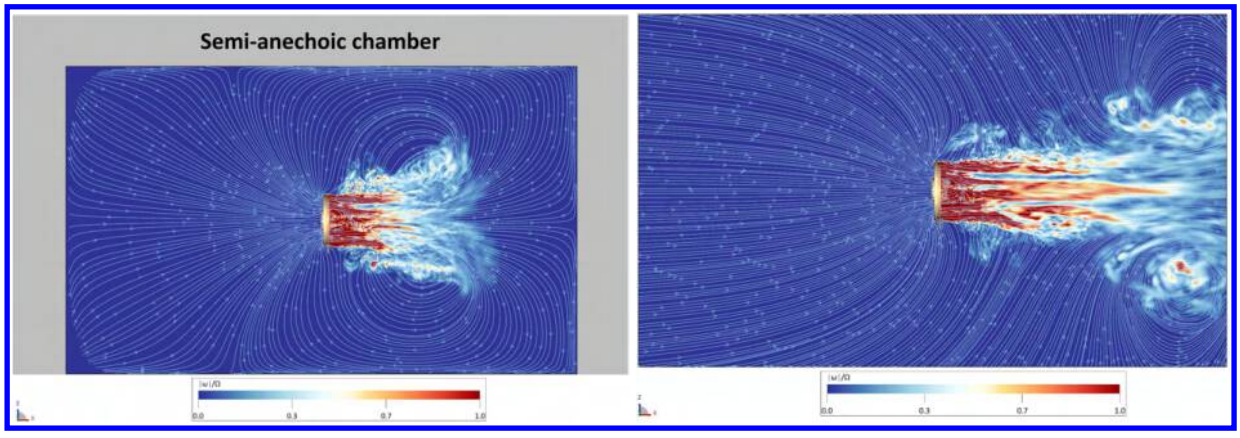

(a) (b)

Fig. 10 Mean vorticity field with streamlines in a plane at $y/D = 0$ (free blowing conditions). (a): Semi-anechoic chamber. (b): Free field.

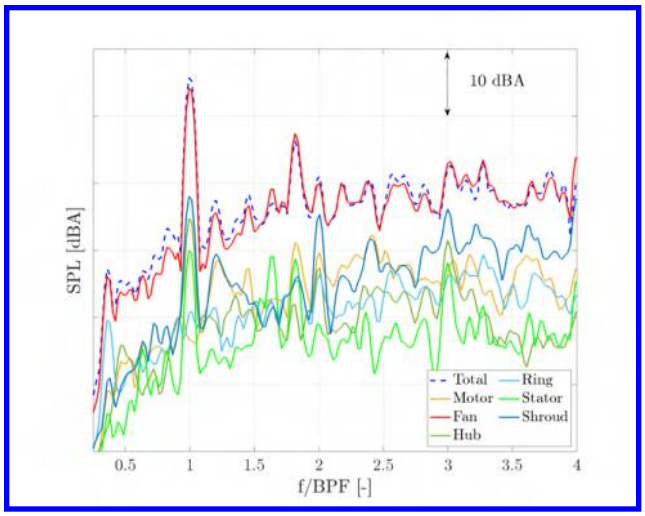

Fig. 11 Surfaces contribution $2.15D$ upstream at the probe aligned with the fan axis obtained through the FWH solid formulation. Every contribution is colored according to Fig. 1a.

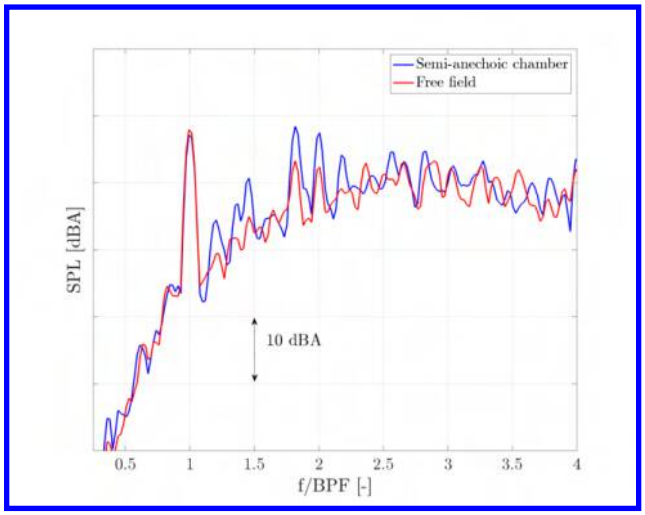

Fig. 12 Pressure fluctuations $2.15D$ upstream at the probe aligned with the fan axis (free blowing conditions).

stated that the unsteady loading fluctuations, mainly due to an installation effect, in the free blowing operating condition, are the main responsible for the acoustic pressure spectral pattern recorded $2.15D$ upstream along the fan axis.

The free field effect is seen mainly as a reduction of the peak at $f/BPF = 2$ of $6.3\,dBA$, and the sub-harmonic humps, while the tone at $f/BPF = 1$ remains unchanged, as shown in Fig. 12. Starting from $f/BPF > 2$ it can be observed a slight shift of the valleys to higher frequencies, as well as the vanishing of the hump at $f/BPF = 2.6$. Due to this, the overall SPL is reduced by about $1\,dBA$. The reason behind the observed differences on the peaks might rely upon the fact that, due to the recirculation in the semi-anechoic chamber, the fan inflow carries with it a higher turbulent content. This has also been found by Sturm et al. [26] when comparing their results, on the same fan geometry, with Zhu [44]. It has been shown that, by allowing the flow to fully develop in the room, tones at the BPF harmonics arise. In the present work, however, the tone at the BPF is present anyway, since it has been assessed to be due to an installation effect.

B. Operating condition effects

The operating condition effect is assessed by comparing the numerical results from the free blowing and maximum efficiency conditions in the free field domain. The free blowing setup has been slightly modified by introducing the solid

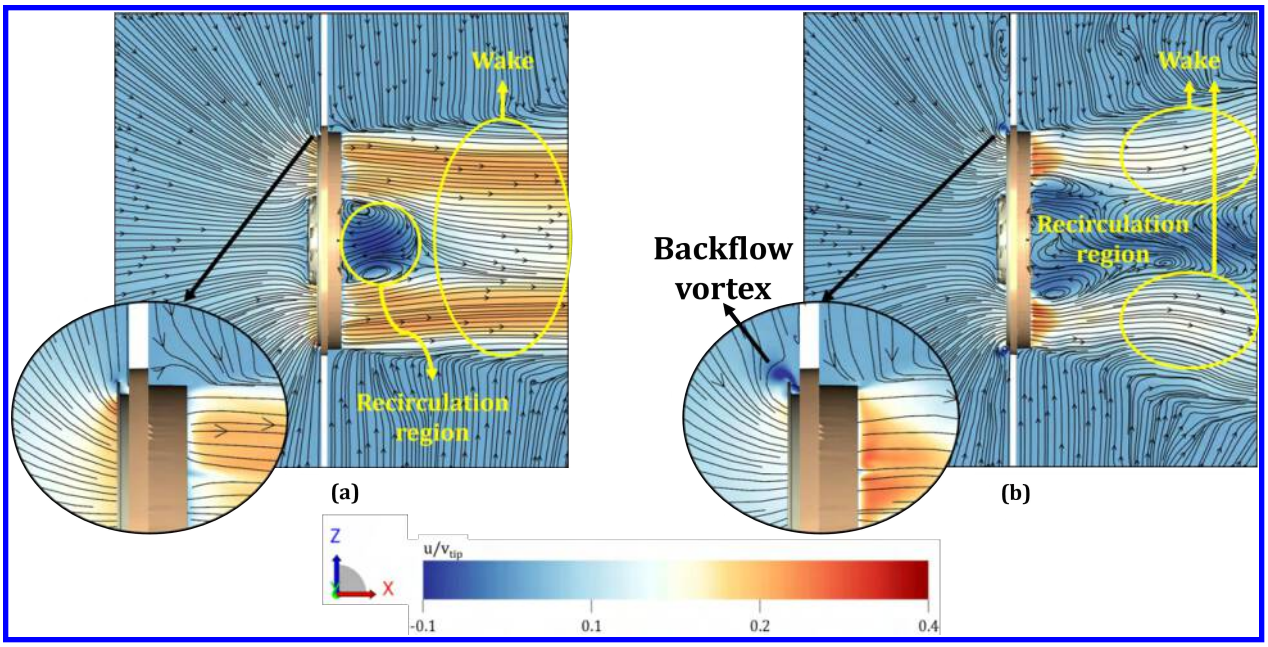

Fig. 13 Mean axial velocity for the free blowing and maximum efficiency operating points in a plane located at $y/D = 0$ (free field domain). (a): Free blowing. (b): Max efficiency.

wall that has been shown in Sec. V. This did not result in significant variations on the noise footprint of the cooling module, comparing to the free blowing free field setup without the thin wall.

1. Aerodynamic results

Flow field topology changes reasonably, as shown in Fig. 13. It is seen firstly that, in free blowing conditions, the wake is convected downstream with high speed and without any deviation, while at maximum efficiency the wake is characterized by lower velocity and a broader recirculation region. This can be attributed to the fact that free blowing conditions are characterized by a higher mass flow rate (i.e. higher axial velocity) and nearly zero flow resistance (there's no pressure difference between upstream and downstream), unlike the best efficiency point, as mentioned before and as also found by Kim et al. [45]. It can be also detected a backflow vortex located on the blade ring at maximum efficiency, generated by the pressure difference across the fan. Indeed, such pressure difference causes a backflow in the tip gap region which increases from 3% (free blowing) to 10.5% (max efficiency) of the mass flow rate of the corresponding operating point.

This vortex interacts with the blades' leading edge, in the tip region, causing strong wall pressure fluctuations, as highlighted in Fig. 14. It can be seen also that hub secondary flows are present and that there's no separation anymore in this operating condition, as confirmed by the pressure coefficient distribution in Fig. 15a since the incidence seen by the blades is decreased with respect to the free blowing point.

Therefore, blade loading is characterized by a higher broadband content on all the frequencies of interest and also by a lower intensity at $f/BPF = 1$, as visible in Fig. 15b. The latter is mainly because the localized flow blockage seen before is no longer present, as shown in Fig. 16. There's an azimuthally uniform low-speed region instead, mainly due to the hub secondary flows discussed before.

2. Acoustic results

Fig. 17 shows that the maximum efficiency condition is characterized by a higher broadband level and a tone at $f/BPF = 1$ that is 7.7 dBA lower; there's also a peak 8.09 dBA higher at $f/BPF = 2$. The maximum efficiency condition increases the overall SPL by 1.08 dBA against the free blowing case.

By analyzing the axial velocity spectral content on a probe located in the ring region (Fig. 18a) it can be seen in Fig. 18b that, even if the maximum efficiency condition has a lower mean axial velocity (due to the lower mass flow rate), it is characterized by higher fluctuations, with a peak between $f/BPF = 1$ and $f/BPF = 2$ that is visible also in the

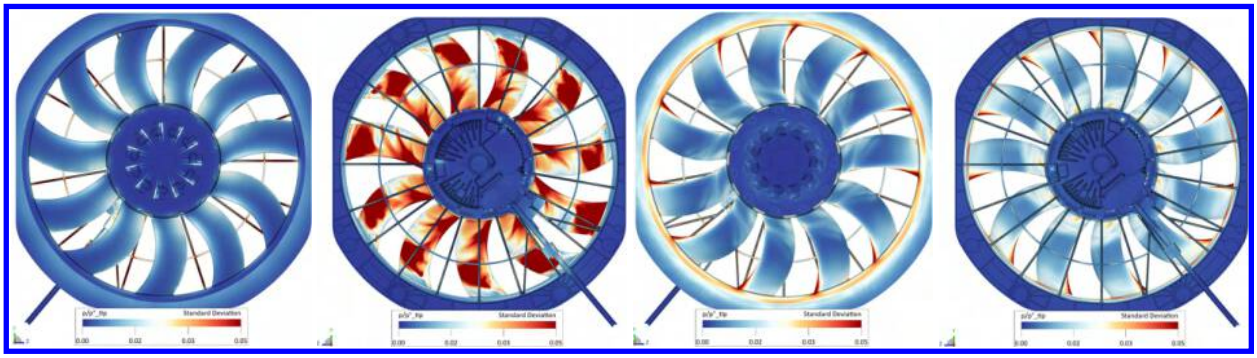

(a) (b) (c) (d)

Fig. 14 Surface pressure standard deviation on the fan for the free blowing and maximum efficiency operating points (free field domain). (a): Free blowing (front). (b): Free blowing (rear). (c): Max efficiency (front). (d): Max efficiency (rear).

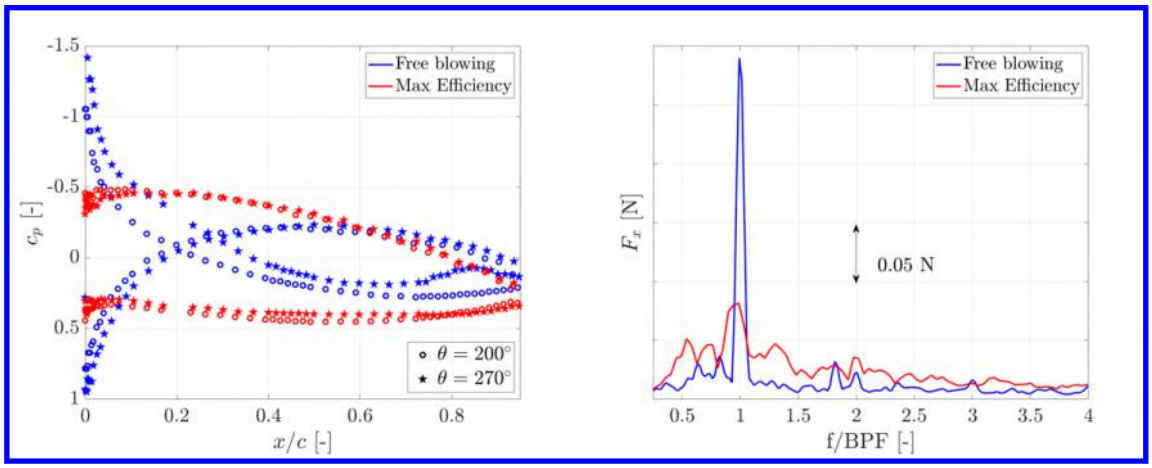

(a) (b)

Fig. 15 Pressure coefficient and loading spectrum for the free blowing and maximum efficiency operating points (free field domain). (a): Pressure coefficient of one blade at two different θ locations. $\theta = 200°$ corresponds to the blockage region. (b): Spectrum of the loading given by all the 11 blades.

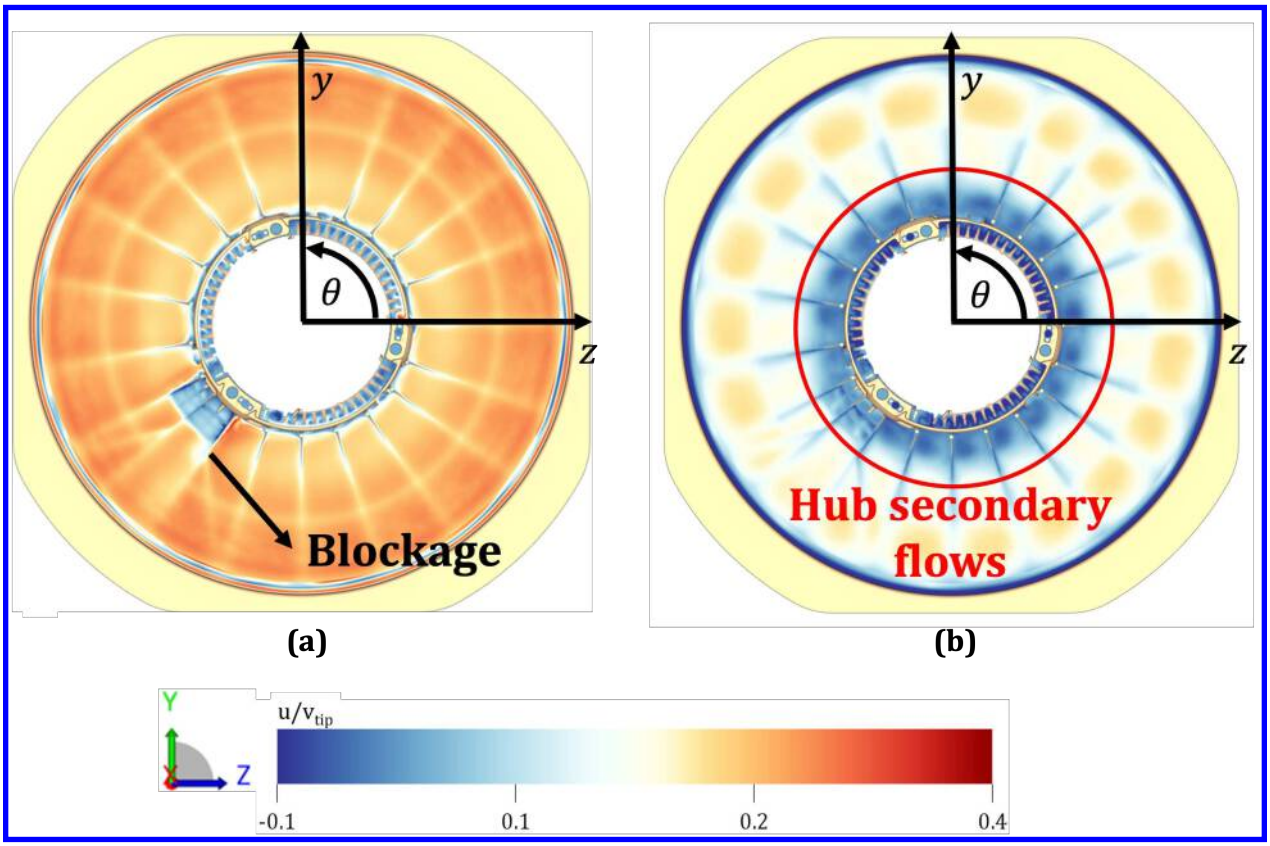

Fig. 16 Mean axial velocity in a plane located at $x/D = -0.06$ (free field domain). (a): Free blowing. (b): Max efficiency.

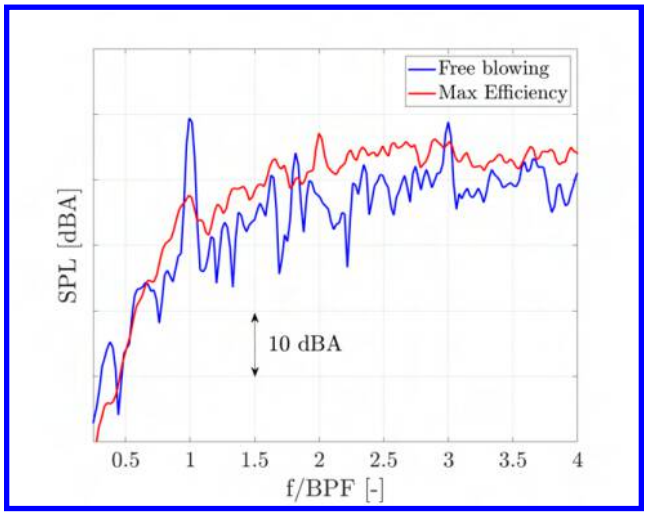

Fig. 17 Pressure fluctuations $2.15D$ upstream at the probe aligned with the fan axis for the free blowing and maximum efficiency operating points (free field domain).

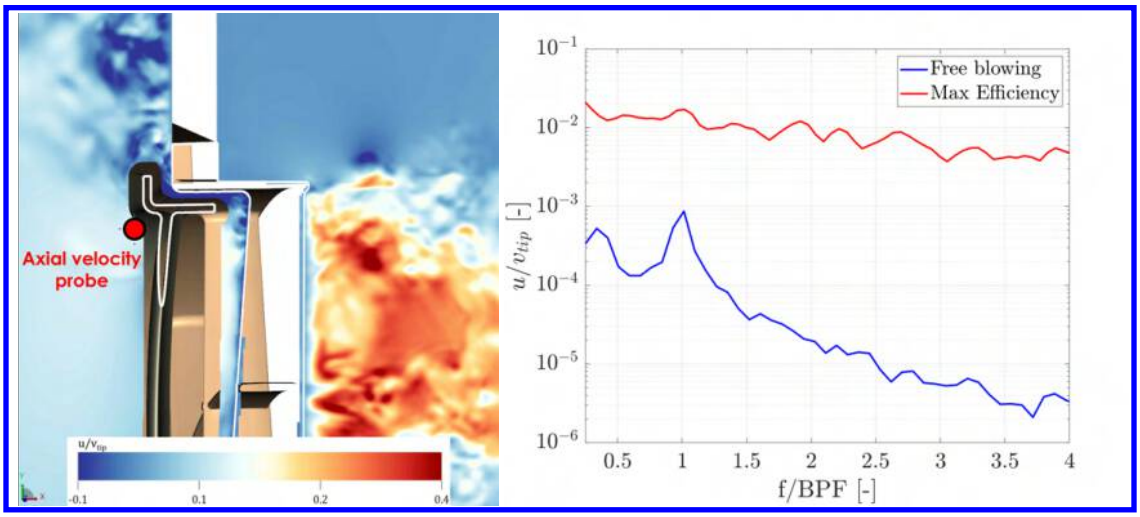

(a) (b)

Fig. 18 Axial velocity fluctuations near the tip for the free blowing and maximum efficiency operating points (free field domain). (a): Location of the probe where the axial velocity is sampled. (b): Axial velocity fluctuations in the ring region, the probe location is shown in Fig. 18a.

pressure fluctuations spectrum. This explains the noise footprint of this different operating conditions and highlights that there can be significant differences in the flow field, with non-negligible changes in the acoustic emissions of the cooling module.

To further demonstrate what has been stated in this section, fan surface noise contribution at a given microphone location has been computed through the OptydB-pfnoisescan [46] tool. The resulting surface field is shown in frequency bands centered at $f/BPF = 1$ and $f/BPF = 2$ as dB/m^2. At $f/BPF = 1$ (Fig. 19) the main contributions for the maximum efficiency case are located on the tip leading edge of the blades and the corresponding ring regions, highlighting the interaction of the upstream recirculation vortex with the fan. Conversely, at free blowing conditions, the main contribution is located on the blades' pressure side, more precisely in the near hub region, where the incidence is higher (and so is the separation), and concurrently where the blockage occurs due to the cable strut.

Differently, at a frequency of $f/BPF = 2$, it is seen that the predominant surface source at maximum efficiency is located on the pressure side of the blades, with a further contribution of the ring and both tip leading and trailing edges of some blades. The latter can be attributed to the upstream recirculation, as depicted in Fig. 18b. At the same time, the former should be considered to be caused by the potential effect of the rotor-stator interaction. It can be recognized a loading hump on the spectrum in Fig. 15b at $f/BPF = 2$ which might arise because of the simultaneous interaction of all the blades with two stator vanes along a blade chord. This would generate a blade loading peak $2N_b$ times in a fan rotation, yielding a loading peak at a frequency of $2N_b\Omega = 2BPF$. This will be further investigated in the following works. At free blowing conditions, instead, the major contribution is seen only on the pressure side, due to the interaction of the stalled blades with the stator vanes. Indeed, blades cannot be as much sensitive to the slight loading hump at $f/\Omega = 20$ since they are experiencing the boundary layer separation discussed before.

VIII. Conclusions

This study reports a comprehensive numerical investigation into the noise sources associated with an industrial engine cooling fan under various operating conditions. The research has shed light on the spatial and frequency characteristics of these noise sources and their sensitivity to different environmental and operational factors.

In the semi-anechoic chamber at free-blowing conditions, numerical simulations demonstrated good agreement with experimental data when employing finer grid resolutions. It has been identified that the predominant noise source is related to local flow blockage which locally alters the blade loading, resulting in a peak at the blade passing frequency. In this condition, the flow over the blades is mainly separated. This installation effect is a crucial consideration in noise assessment for such fans. When the semi-anechoic chamber is removed, transitioning to a free field environment, it has been observed a reduction in the harmonics of the blade passing frequency in the far-field acoustic pressure, as well

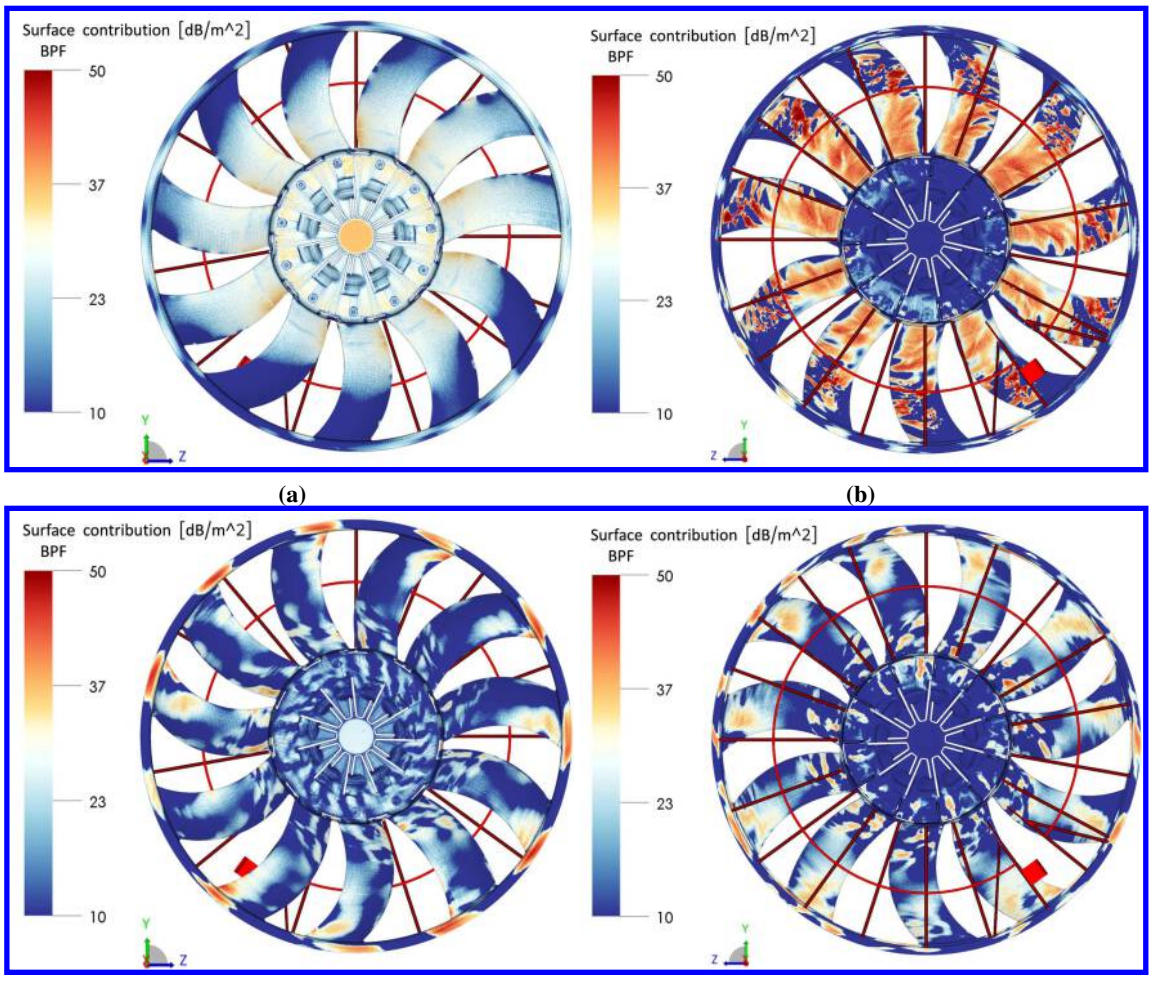

Fig. 19 Surface noise contribution $2.15D$ upstream at the probe aligned with the fan axis and at $f/BPF = 1$ for the free blowing and maximum efficiency operating points (free field domain). (a): Free blowing (front plane). (b): Free blowing (rear plane). (c): Max efficiency (front plane). (d): Max efficiency (rear plane).

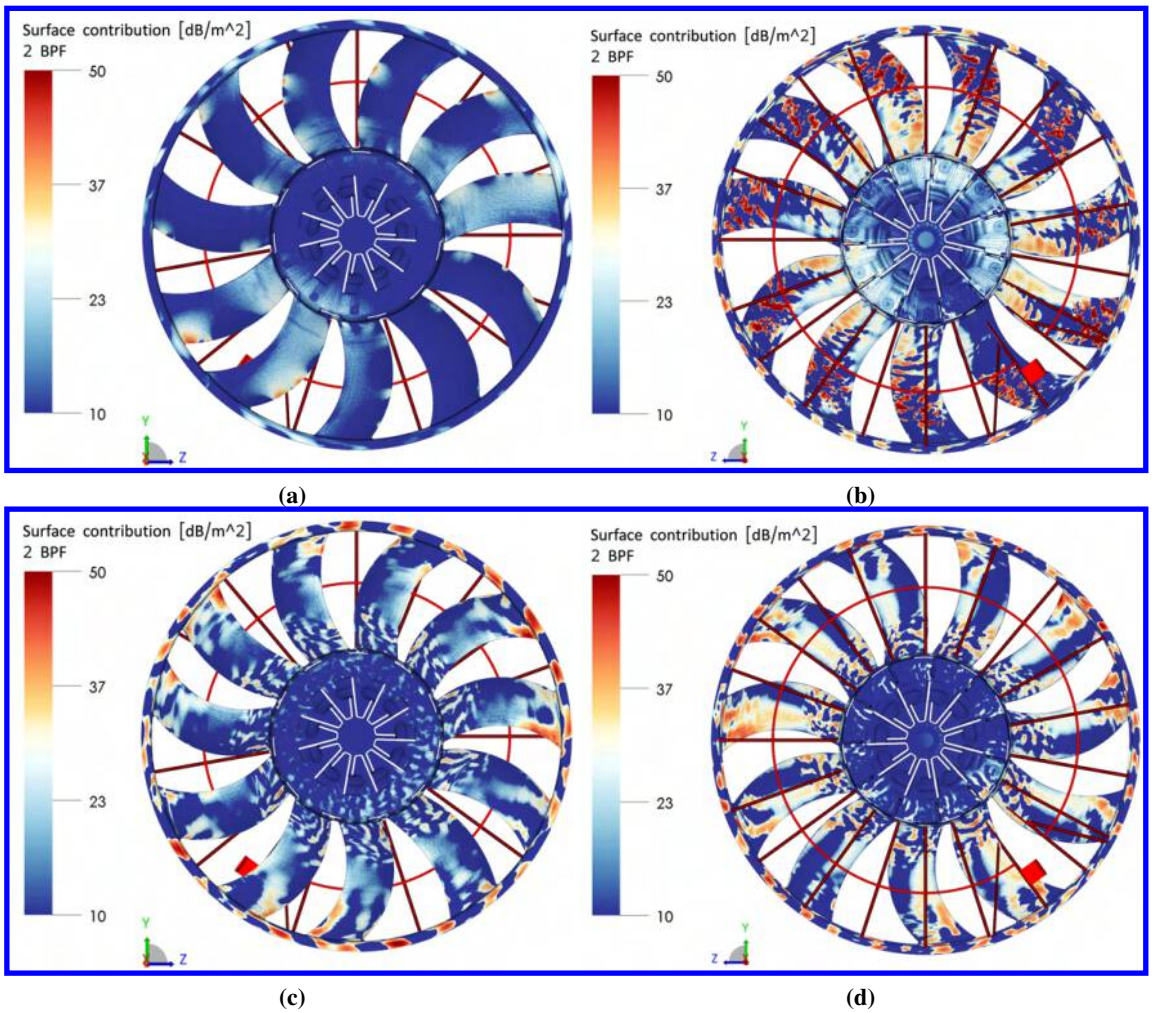

Fig. 20 Surface noise contribution $1\,m$ upstream at the probe aligned with the fan axis and at $f/BPF = 2$ for the free blowing and maximum efficiency operating points (free field domain). (a): Free blowing (front plane). (b): Free blowing (rear plane). (c): Max efficiency (front plane). (d): Max efficiency (rear plane).

as in a few of the sub-harmonic humps. This reduction was attributed to the absence of recirculation, emphasizing the significance of environmental conditions on noise propagation. At the fan's maximum efficiency point, where a pressure difference across the fan was introduced, the generation of a stationary recirculation vortex in the fan's ring region became the main noise generation mechanism. This vortex interacts with the blades' tip leading edges, resulting in an acoustic spectrum showing a higher broadband content on all the frequencies of interest and a lower tone at the BPF. This was enhanced by the flow distribution over the blades, which is now mostly attached, so there is no separation anymore. In addition, a tone at the BPF's first harmonic is seen, probably generated by the simultaneous potential interaction between every blade and two stator vanes over a blade chord. Under boundary layer separation it wouldn't be possible for the blades to be sensitive to this slight loading hump.

Future research will focus on the development of noise reduction techniques for the same fan geometry, aiming to mitigate noise emissions without compromising aerodynamic efficiency. Additionally, the introduction of a heat exchanger upstream will be investigated, as this modification may influence noise generation characteristics. This will contribute to quieter and more efficient fan designs, meeting the demands of both industry and environmental sustainability.

References

[1] Piwowarski, M., and Jakowski, D., "Areas of fan research—A review of the literature in terms of improving operating efficiency and reducing noise emissions," *Energies*, Vol. 16, No. 3, 2023, p. 1042.

[2] Moreau, S., "The third golden age of aeroacoustics," *Physics of Fluids*, Vol. 34, No. 3, 2022, p. 031301.

[3] Díaz, A. K. M., Fernández, O. J. M., Marigorta, E. B., and Morros, C. S., "Numerical prediction of tonal noise generation in an inlet vaned low-speed axial fan using a hybrid aeroacoustic approach," *Proc Inst Mech Eng Part C*, Vol. 223, No. 9, 2009, pp. 2081–2098.

[4] Cattanei, A., Mazzocut Zecchin, F., Di Pasquali, A., and Lazari, A., "Effect of the uneven blade spacing on the noise annoyance of axial-flow fans and side channel blowers," *Appl. Acoust.*, Vol. 177, No. 107924, 2021, p. 107924.

[5] Yoshida, K., Semura, J., Kohri, I., and Kato, Y., "Reduction of the BPF Noise Radiated from an Engine Cooling Fan," *SAE Technical Paper Series*, SAE International, 2014.

[6] Chaitanya, P., and Joseph, P., "Slitted leading edge profiles for the reduction of turbulence-aerofoil interaction noise," *J. Acoust. Soc. Am.*, Vol. 143, No. 6, 2018, p. 3494.

[7] Ocker, C., Czwielong, F., Chaitanya, P., Pannert, W., and Becker, S., "Aerodynamic and aeroacoustic properties of axial fan blades with slitted leading edges," *Acta Acustica*, Vol. 6, 2022, p. 48.

[8] Zhou, W., Zhou, P., Xiang, C., Wang, Y., Mou, J., and Cui, J., "A review of bionic structures in control of aerodynamic noise of centrifugal fans," *Energies*, Vol. 16, No. 11, 2023, p. 4331.

[9] Sun, Z., Tian, J., Zhang, T., Du, Z., and Ouyang, H., "Cooling fan aerodynamic noise reduction with short inlet duct and its applicability," *Int. J. Refrig.*, Vol. 148, 2023, pp. 117–130.

[10] Ocker, C., Geyer, T. F., Czwielong, F., Krömer, F., Pannert, W., Merkel, M., and Becker, S., "Permeable leading edges for airfoil and fan noise reduction in disturbed inflow," *AIAA J.*, Vol. 59, No. 12, 2021, pp. 4969–4986.

[11] Peng, Z., Wu, Y., Tian, J., and Ouyang, H., "Discrete noise control of cooling fan module: Stator and rotor interaction," *Appl. Acoust.*, Vol. 165, No. 107308, 2020, p. 107308.

[12] Pestana, M., Sanjosé, M., Moreau, S., Roger, M., and Gruber, M., "Investigation on the noise of an axial low Mach-number fan stage with a heterogeneous stator," 2018.

[13] Pestana, M., "Effets de stators hétérogénes sur le bruit d'interaction rotor-stator : étude analytique, expérimentale et numérique," Ph.D. thesis, Université de Lyon, 2020.

[14] Tyler, J. M., and Sofrin, T. G., "Axial flow compressor noise studies," *SAE Technical Paper Series*, SAE International, 400 Commonwealth Drive, Warrendale, PA, United States, 1962.

[15] Zhu, T., Lallier-Daniels, D., Sanjosé, M., Moreau, S., and Carolus, T., "Rotating coherent flow structures as a source for narrowband tip clearance noise from axial fans," *Journal of Sound and Vibration*, Vol. 417, 2018, pp. 198–215.

[16] Marsan, A., Lallier-Daniels, D., Sanjosé, M., Moreau, S., and Mann, A., "Tip leakage flow and its implication on the acoustic signature of a low-speed fan," 2018.

[17] Magne, S., Moreau, S., and Berry, A., "Subharmonic tonal noise from backflow vortices radiated by a low-speed ring fan in uniform inlet flow," *The Journal of the Acoustical Society of America*, Vol. 137, No. 1, 2015, pp. 228–237.

[18] Ghodake, D., Sanjosé, M., Moreau, S., and Henner, M., "Effect of Sweep on Axial Fan Noise Sources Using the Lattice Boltzmann Method," *International Journal of Turbomachinery, Propulsion and Power*, Vol. 7, No. 4, 2022, p. 34.

[19] Feng, J., Bian, T., Han, Q., and Wang, B., "A numerical investigation on the influence of the circular ring on the aerodynamic noise generated by a cooling fan," *FDMP Fluid Dyn. Mater. Process.*, Vol. 19, No. 1, 2023, pp. 1–14.

[20] Piellard, M., Coutty, B. B., Goff, V. L., Vidal, V., and Perot, F., "Direct aeroacoustics simulation of automotive engine cooling fan system: effect of upstream geometry on broadband noise," *20th AIAA/CEAS Aeroacoustics Conference*, American Institute of Aeronautics and Astronautics, 2014.

[21] Kohout, D., and Hyhlik, T., "Influence of the shroud leading edge shape on the axial-fan noise," *Proceedings of the 6th World Congress on Mechanical, Chemical, and Material Engineering*, Avestia Publishing, 2020.

[22] Benedek, T., Vad, J., and Lendvai, B., "Combined acoustic and aerodynamic investigation of the effect of inlet geometry on tip leakage flow noise of free-inlet free-exhaust low-speed axial flow fans," *Applied Acoustics*, Vol. 187, 2022, p. 108488.

[23] Zhu, T., and Carolus, T. H., "Axial fan tip clearance noise: Experiments, Lattice-Boltzmann simulation, and mitigation measures," *International Journal of Aeroacoustics*, Vol. 17, No. 1-2, 2018, pp. 159–183.

[24] Lallier-Daniels, D., Piellard, M., Coutty, B., and Moreau, S., "Aeroacoustic study of an axial engine cooling module using lattice-Boltzmann simulations and the Ffowcs Williams and Hawkings' analogy," *European Journal of Mechanics - B/Fluids*, Vol. 61, 2017, pp. 244–254.

[25] Foss, J., Neal, D., Henner, M., and Moreau, S., "Evaluating CFD models of axial fans by comparisons with phase-averaged experimental data," *SAE Technical Paper Series*, SAE International, 400 Commonwealth Drive, Warrendale, PA, United States, 2001.

[26] Sturm, M., Sanjose, M., Moreau, S., and Carolus, T., "Aeroacoustic simulation of an axial fan including the full test rig by using the lattice boltzmann method," *FAN 2015 : International Conference on Fan Noise, Technology and Numerical Methods*, Institution of Mechanical Engineers, London, 2015.

[27] Longhouse, R. E., "Noise mechanism separation and design considerations for low tip-speed, axial-flow fans," *J. Sound Vib.*, Vol. 48, No. 4, 1976, pp. 461–474.

[28] He, X., and Luo, L.-S., "Theory of the lattice Boltzmann method: From the Boltzmann equation to the lattice Boltzmann equation," *Phys. Rev. E Stat. Phys. Plasmas Fluids Relat. Interdiscip. Topics*, Vol. 56, No. 6, 1997, pp. 6811–6817.

[29] Sanjose, M., Lallier-Daniels, D., and Moreau, S., "Aeroacoustic Analysis of a Low-Subsonic Axial Fan," 2015.

[30] Perot, F., Moreau, S., Kim, M.-S., Henner, M., and Neal, D., "Direct aeroacoustics predictions of a low speed axial fan," *16th AIAA/CEAS Aeroacoustics Conference*, American Institute of Aeronautics and Astronautics, 2010.

[31] Perot, F., Kim, M.-S., Moreau, S., and Henner, M., "Axial fan noise aeroacoustics predictions and inflow effect on tonal noise using LBM," 2013.

[32] Bhatnagar, P. L., Gross, E. P., and Krook, M., "A model for collision processes in gases. I. small amplitude processes in charged and neutral one-component systems," *Phys. Rev.*, Vol. 94, No. 3, 1954, pp. 511–525.

[33] Chapman, S., and Cowling, T. G., *Cambridge mathematical library: The mathematical theory of non-uniform gases: An account of the kinetic theory of viscosity, thermal conduction and diffusion in gases*, Cambridge University Press, Cambridge, England, 1991.

[34] Qian, Y. H., D'Humières, D., and Lallemand, P., "Lattice BGK models for Navier-stokes equation," *EPL*, Vol. 17, No. 6, 1992, pp. 479–484.

[35] Zhang, R., Sun, C., Li, Y., Satti, R., Shock, R., Hoch, J., and Chen, H., "Lattice Boltzmann approach for local reference frames," *Commun. Comput. Phys.*, Vol. 9, No. 5, 2011, pp. 1193–1205.

[36] Chen, H., Kandasamy, S., Orszag, S., Shock, R., Succi, S., and Yakhot, V., "Extended Boltzmann kinetic equation for turbulent flows," *Science*, Vol. 301, No. 5633, 2003, pp. 633–636.

[37] Teixeira, C. M., "Incorporating turbulence models into the Lattice-Boltzmann method," *Int. J. Mod. Phys. C.*, Vol. 09, No. 08, 1998, pp. 1159–1175.

[38] Launder, B. E., and Spalding, D. B., "The numerical computation of turbulent flows," *Comput. Methods Appl. Mech. Eng.*, Vol. 3, No. 2, 1974, pp. 269–289.

[39] Williams, J. E. F., and Hawkings, D. L., "Sound generation by turbulence and surfaces in arbitrary motion," *Philos. Trans. R. Soc. Lond.*, Vol. 264, No. 1151, 1969, pp. 321–342.

[40] Casalino, D., "An advanced time approach for acoustic analogy predictions," *J. Sound Vib.*, Vol. 261, No. 4, 2003, pp. 583–612.

[41] Farassat, F., and Succi, G. P., "The prediction of helicopter rotor discrete frequency noise," *ahs*, 1982, pp. 497–507.

[42] Richardson, L. F., "The approximate arithmetical solution by finite differences of physical problems involving differential equations, with an application to the stresses in a masonry dam," *Philos. Trans. R. Soc. Lond.*, Vol. 210, No. 459-470, 1911, pp. 307–357.

[43] Lallier-Daniels, D., Moreau, S., and Sanjose, M., "Aeroacoustics of a Low-Speed Free Tip Fan With a Complex Clearance Geometry," *Volume 13: Vibration, Acoustics and Wave Propagation*, American Society of Mechanical Engineers, 2014.

[44] Zhu, T., and Carolus, T., "Experimental and numerical investigation of tip clearance noise of an axial fan using a lattice boltzmann method," FAN, 2015.

[45] Kim, M.-S., Pérot, F., Mann, A., Choi, E.-S., Cho, M.-H., and Kim, J.-H., "Automotive engine cooling fan noise prediction using a Lattice Boltzmann based Method," FISITA World Congress, 2016.

[46] Casalino, D., Grande, E., Romani, G., Ragni, D., and Avallone, F., "Definition of a benchmark for low Reynolds number propeller aeroacoustics," *Aerosp. Sci. Technol.*, Vol. 113, No. 106707, 2021, p. 106707.